Surface Characterization of TiO_2 Polymorphic Nanocrystals through ^{1}H-TD-NMR

Massimo Tawfilas,† Michele Mauri,† Luca De Trizio,‡ Roberto Lorenzi,†and Roberto Simonutti,†*

† Department of Materials Science, University of Milano-Bicocca, via R. Cozzi 55, 20125 Milan, Italy

‡ Istituto Italiano di Tecnologia, Via Morego 30, 16163 Genova, Italy

** Corresponding author: roberto.simonutti@unimib.it*

Abstract

Nanocrystals (NCs) surface characterization is a fundamental step for understanding the physical and chemical phenomena involved at the nanoscale. Surface energy and chemistry depend on particle size and composition, and, in turn, determine the interaction of NCs with the surrounding environment, their properties and stability, and the feasibility of nanocomposites. This work aims at extracting more information on the surface of different titanium dioxide polymorphs using 1H-TD-NMR of water. Taking advantage of the interaction between water molecules and titanium dioxide NCs, it is possible to correlate the proton transverse relaxation times (T2) as the function of the concentration and the specific surface area (δp·Cm) and use it as an indicator of the crystal phase. Examples of three different crystals phase, rutile, anatase, and brookite, have been finely characterized and their behavior in water solution have been studied with TD-NMR. The results show a linear correlation between relaxivity (R2) and their concentration Cm. The resulting slopes, after normalization for the specific surface, represent the surface/water interaction and range from 1.28 g m–2 s–1 of 50 nm rutile nanocrystals to 0.52 for similar sized brookite. Even higher slopes (1.85) characterize smaller rutile NCs, in qualitative accordance with the trends of surface energy. Thanks to proton relaxation phenomena that occur at the NCs surface, it is possible to differentiate the crystal phase and the specific surface area of titanium dioxide polymorphs in water solution.

Introduction

Nanocrystals often display interesting properties, different from those of bulk materials of similar composition. In ferromagnetic NCs smaller than the bulk magnetic domain size, the phenomenon of superparamagnetism appears, (1) which can be exploited for biomedical applications such as the improvement of magnetic resonance imaging (2,3) or hyperthermal treatment of cancer cells. (4) Size reduction can also bring significant quantomechanical properties such as the quantized conductivity of nanowires or the enhanced luminescence of Si quantum dots. (5) Bioactivity is also influenced by crystal size and shape, (6) both at cellular and systemic level; for example, silver NCs are effective bactericides, (7) whereas renal clearance of non-biodegradable particles is limited to few nanometer CdSe/ZnS quantum dots. (8)

At the nanoscale, the surface-to-volume ratio of the materials becomes preponderant and the surface effects play a major role in determining the properties of the NC. (9) In many cases, a proper surface modification of NCs is strongly required to avoid segregation (10) and thus produce viable nancomposites. Surface decoration is the main strategy to ensure optimal mixing of graphene, (11) silica, (12) or clays (13) within the polymer matrices, producing materials with optimized properties. Interaction with cells, including internalization and cytotoxicity, is also influenced by surface functionality even more than size. (14)

TiO2 in the form of NCs is routinely used in dye-sensitized solar cells (15) or dispersed in a solid polymer matrix, endowing it with enhanced mechanical, (16) optical, (17) or electrical (18) properties. Different properties are associated with different phases of titanium dioxide; for example, rutile is distinguished for its higher permittivity constant compared to anatase, (19) and thus significant efforts were made to synthesize phase pure TiO2 NCs. (20) Toxicity can also depend on the polymorph, (21) a relevant issue considering the amount used in food. (22)

In this work, we explore the application of time domain NMR (TD-NMR) to characterize the surface of TiO2 nanoparticles, adding a new point of view to the wide diversity of methods commonly employed in the field of NCs characterization.

To date, dynamic light scattering (DLS) is the most used technique for measuring the size distribution of NCs in the solution, (23) often coupled with the ζ-potential surface charge measurement. Scanning and transmission electron microscopies (SEM, TEM) and X-ray diffraction (XRD) are widely used for determining the morphology (size and shape) and the crystal structure of the NCs. The Brunauer–Emmett–Teller (BET) analysis allows quantification of the specific NCs' surface area, whereas Fourier transform infrared (FTIR) spectroscopy, (24) high field nuclear magnetic resonance (NMR), (25) X-ray photoelectron spectroscopy, and elemental analysis can be used for characterizing the nature and the binding modes of surface ligands.

Time domain (TD) NMR, a technique based on the same principles as modern (pulsed) NMR, involves direct study of the free induction decay signal without the Fourier transform. Interestingly, using TD-NMR, it is possible to measure the effect on the proton transverse relaxation times, 1H T2, of water exerted by the dispersed NCs as a function of the total accessible surface.

In this work, we demonstrate for the first time that 1H-TD-NMR is able to differentiate the surface of TiO2 NCs of the three different polymorphic crystal structures: anatase, brookite, and rutile. We selected TiO2 as the subject of our study, as it can be synthesized at the nanoscale with a high control over the size, shape, and crystal structure. Rutile, anatase, and brookite TiO2 NCs were either synthesized or acquired and fully characterized via DLS, XRD, TEM, and BET analyses.

1H T2 Relaxation of Nanocrystal Dispersions

Relaxation of nuclear spin magnetization of solvents in the presence of paramagnetic iron or manganese NCs has been studied in depth due to important applications as contrast agent for magnetic resonance imaging. (2) More recently, other paramagnetic nuclei have also been exploited to reduce spin lattice relaxation times, as in the case of gadolinium(III) diethylenetriaminepentacetate used to lessen the experimental time required to acquire 13C CPMAS spectra of bone samples (26) or copper-chelated lipid to significantly enhance the sensitivity of an NMR experiment on lipid bilayers. (27)

Where the disperse phase contains protons, as in the case of emulsions, mobility contrast is often present and methods based on pulsed field gradient are applicable to decouple local motions from the translational motion of the particles, thus determining their size. (28) Time domain NMR can also be applied to directly determine the internal dynamic state of the disperse phase. (29)

Even in the absence of a strong and long-range relaxing effect due to the local magnetic field gradient generated by paramagnetic domains, short-range interaction with the NCs leads to relaxation. Namely, the solvent molecules interacting with the NCs surface have a restricted mobility compared to the noninteracting ones, and dipolar interactions with surface groups or other adsorbed particles can bring a rapid decrease in the transverse magnetization.

In the framework of the relaxation theory (30,31) based on the seminal work of Redfield, (32) comprehensive models describing the relaxation of interacting and noninteracting solvents have been proposed in the literature, and also used to estimate the size of diamagnetic inorganic particles such as silica and the interaction between NCs and polymers, including qualitative and quantitative measurements of absorption of polymers on the surface. (33,34) This concept has growing applications in the characterization of cements (35) and carbon fillers (36) and has recently been refined to include the study of particle shape (37) or the coverage. (38)

Even though the mechanisms that induce NMR relaxation are still debated, (39) with possibly complementary effects due to dipolar interaction and motional constraint, most interpretative models describe solvent as a two-phase system composed of a population of molecules bound to the particle surface and a population of bulk solvent, as depicted in Figure 1.

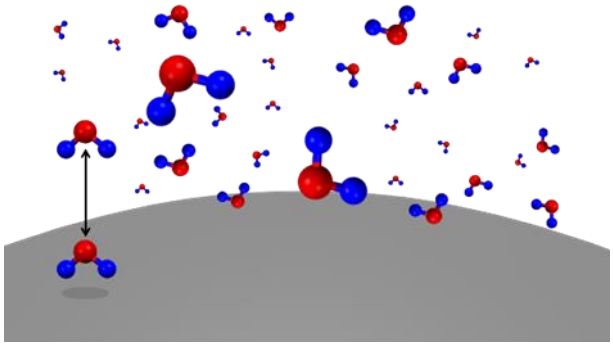

Figure 1. Representation of the interaction between water molecule and a generic nanocrystal. The arrows indicate the dynamic exchange between the bound phase and the free solvent. Free water molecules are shown blurred to indicate their high mobility.

For analytical treatment of the resulting NMR relaxation, we define Pb and Pf as the probabilities to find a proton in the interacting (bound) and noninteracting (free) phase at a given time, vb and vf as the rates at which a solvent molecule leaves the two phases, and Rb and Rf as the NMR relaxation rates of the two phases, respectively. At equilibrium, vb = vf and the relaxation curve can be analytically determined according to the fast-exchange (vb $\gg$ Rb and vf $\gg$ Rf) or slow-exchange model (vb $\ll$ Rb and vf $\ll$ Rf). In the first case, a single exponential decay is observed, and the relaxation rate R is given by the average of the relaxation rates, weighed by the probability of occupying each phase

$$R = P_b R_b + (1 - P_b) R_f$$

(1)

However, in the slow-exchange regime, the predicted relaxation curve is bimodal and constituted by the summation of separate contributions from the free and bound protons

$$I(t) = I_0\left(P_b e^{-R_b t} + P_f e^{-R_f t}\right).$$

(2)

This simple expression, where I0 and I(t) represent the intensity at t = 0 and at time t, respectively, is substituted by a multimodal curve or even a continuous distribution in case different populations of particles or environments are present, as in nanoporous silica or natural rocks. (40)

Relaxation curves acquired for water dispersions containing TiO2 NCs in this work are well fitted by a single exponential, so the equations will be expressed within the framework of the fast-exchange regime. Because the probability Pb is the ratio between the number of solvent molecules interacting with the surface and the total number of solvent molecules, it can be defined by

$$P_b = C_M \sigma_p \frac{m_s}{N_0} \mu$$

(3)

where CM is the NC mass fraction, σp is their specific surface, ms is the solvent molar mass, N0 is the Avogadro's constant, and μ is the number of solvent molecules bound to the surface per unit surface. For water dispersions, T2 is in the range of seconds and thus the relaxation rate of the free solvent is significantly smaller than that of the bound solvent, and a linear relation between the nanocrystal concentration and the NMR measurable relaxation rate can be easily obtained

$$R = \frac{\sigma_p m_s \mu R_b}{N_0} C_M + R_f$$

(4)

Some previous works (38,41) postulate that each particle binds a layer with a thickness L independent of the particle size, and that the only relevant variable is Rb. We propose an even weaker assumption: the amount of particles per surface unit and the relaxation rate of the same cannot be disentangled. Thus, product μRb defines the surface–solvent interaction as a whole. The most straightforward application is that after a calibration of this parameter for a given system, we can obtain an unknown specific surface area from a known concentration of NCs and vice versa. This basic application can be helpful in evaluating the amount of NCs after a centrifugation or dialysis step. More interestingly, if the specific surface σ can be determined independently from another technique, μRb provides a measure of the solvent–surface interaction, a predictive factor of its catalytic biological activity. For example, it was shown that silica, alumina, and polystyrene particles possess different specific R2 after surface normalization. (41,42) Unsurprisingly, hydrophobic polystyrene surfaces have an almost negligible interaction with water, as compared with silica.

Experimental Section

Reagents

Titanium(IV) butoxide (TB, 97%), titanium(IV) chloride (TiCl4, >99%), oleic acid (OLAC, 90%), oleyl amine (OLAM, 70%), 1-octadecene (ODE, 90%), ammonium hydroxide solution (NH4OH, 28%), absolute ethanol (≥99.8%), hexane (≥95%), dimethylformamide (DMF, ≥99.9%), and water and toluene (≥99.9%) were purchased from Sigma-Aldrich. Nitrosoniumtetrafluoroborate (NOBF4, 98%) was purchased from Alfa Aesar. Rutile NCs were purchased and used as received or hydroxylated as described below. Two different samples with different sizes and specific surface area were acquired: Rut50 was purchased from Sigma-Aldrich (<100 nm diameter, nominal surface area 50 m2 g–1) and Rut20 was purchased by NanoAmor (<50 nm diameter, nominal surface area 160 m2 g–1).

Synthetic Methods

Synthesis of Anatase TiO2 NCs

The synthesis of TiO2 NCs is accomplished using a solvothermal method. (43) Typically, TB (10 mmol) is added to a mixture of 60 mmol OLAC, 40 mmol OLAM, and 11.7 mL absolute ethanol.

The mixture is poured in a 40 mL Teflon beaker and stirred for 15 min before being transferred into a 400 mL Teflon-lined stainless steel autoclave containing 40 mL of a solution of ethanol and water (96% ethanol). The system is then heated to 180 °C for 18 h. The crude product is then centrifuged to precipitate a white powder constituted by titania NCs covered by oleic acid whose polar terminal group is bound to the surface. The aliphatic portion of oleic acid allows easy dispersal in hexane, an apolar solvent. The particles are precipitated several times in ethanol to remove excess ligands and eventually dispersed in hexane.

Synthesis of Brookite TiO2 NCs

TiO2 brookite NCs were synthesized following the procedure reported by Buonsanti et al. (44) In a typical synthesis, a solution of ODE (0.24 mol, 60.6 g), OLAM (0.26 mol, 69.6 g), and OLAC (0.02 mol, 5.65 g) is loaded into a three-neck flask and degassed at 120 °C for 90 min, after which the mixture is cooled down to 50 °C in N2 ambient. TiCl4 (0.02 mol, 3.8 g) is slowly added to the solution and the flask is heated up to 290 °C. The reaction is halted after 30 min and cooled down using an ice bath. The solution is dispersed in hexane and then precipitated several times in 2-propanol and then kept in hexane.

Ligand-Stripping Procedure

A dispersion of TiO2 particles in hexane is added to a solution of NOBF4 and DMF. The resulting biphasic mixture is stirred to maximize the interface where the ligand exchange takes place. As the ligand is

substituted by BF_4^-, the surface polarity changes and NCs are transferred from the nonpolar (hexane) to the (DMF) phase, typically within 60 min. (45,46) The surface-modified NCs are then purified by precipitation with the addition of toluene, which is miscible with DMF, and then the precipitated NCs are dispersed in water. To increase the hydroxyl groups on the NCs surface and have a ligand-free surface, the as-prepared particles are treated with a solution of ammonium hydroxide and stirred for 24 h at 70 °C. (44) After that process, the particles are purified by centrifugation with water till the solution reaches pH 7–9. This process was applied to all TiO_2 samples to avoid different behaviors related to the sample preparation.

Characterization Techniques

Dynamic Light Scattering (DLS)

The hydrodynamic diameter and size distributions of the particles were determined by DLS in deionized water (0.1 mg mL–1). The measures were recorded at 25 °C on a Malvern Zetasizer equipped with a continuous wave 1 mW He–Ne laser operating at 632.8 nm and an avalanche photodiode detector, Q.E. > 50% at 633 nm, placed at 173° with respect to the incident beam. Reported data are the average of at least three different measurements of the size distribution as the function of the intensity.

ζ-Potential

ζ-Potential was measured at 25 °C in deionized water, with a sample concentration of 0.1 mg mL–1 and using a Malvern Zetasizer instrument.

BET

Nitrogen adsorption–desorption isotherms were measured at liquid nitrogen temperature using an ASAP 2010 analyzer (Micrometrics). The samples were outgassed for 12 h at 473 K. The surface area was calculated using the Brunauer–Emmet–Teller (BET) model. (47)

XRD

For X-ray characterization, a D8 Advance powder diffractometer (Bruker) was used with Cu Kα1 radiation (λ = 1.5418 Å) and secondary-beam monochromator. The powder is added on a quartz sample holder and measured.

Micro-Raman

Micro-Raman measurements were carried out at room temperature by a confocal LABRAM (JobinYvon) spectrometer operating in backscattering configuration. The measurements were performed on the samples in a dry powder form. A helium–neon laser (wavelength 632.8 nm, nominal power 17 mW) was used as the exciting source with the spectral resolution of about 2 cm–1. The scattered light was detected

by a CCD (Sincerity, JobinYvon). A microscope (Olympus BX40) was used to focus the excitation on the samples and to collect the scattered radiation with a 20× objective with a numerical aperture of 0.40. The spectra are presented after the baseline subtraction of broad luminescence signals.

Attenuated Total Reflection (ATR)-FTIR

Fourier transform infrared characterization was performed using a PerkinElmer Spectrum 100 instrument scanning from 650 to 4000 cm–1 with a resolution of 4 cm–1 for 64 scans. The sample, in the form of powder, is added on the sample holder and directly analyzed over the Si crystal with the Universal ATR (UATR).

TEM

Bright field TEM (BF-TEM) imaging was performed on a JEOL JEM-1011 microscope equipped with a thermionic gun operating at 100 kV accelerating voltage. For these analyses, the samples were prepared by dropping dilute suspensions of NCs onto carbon-coated 200 mesh copper grids.

TD-NMR

All TD-NMR relaxation experiments were performed at 303 K using a 0.5 T (19.9 MHz proton Larmor frequency) Bruker Minispec mq20 NMR spectrometer equipped with a BVT3000 temperature control system working with nitrogen gas. The temperature was calibrated using an external thermometer with an accuracy of 1 K. The precision is 0.1 K and the temperature is stable within that range during the measurements. All the nanoparticles were studied at different concentrations by preparing a stock dispersion at high concentration and then performing separate dilutions. For each concentration, we inserted 0.15 mL of water dispersion in a 10 mm NMR tube and sonicated it before taking measurements. For the measurement of the transverse relaxation curve of water protons, the Carr–Purcell–Meiboom–Gill (CPMG) pulse sequence was used, acquiring 3000 points with a spacing of 4 ms between successive echoes with a full phase cycle and averaging with at least 16 scans.

Energy-Dispersive X-ray Fluorescence (EDXRF) Analysis

Trace element analysis was performed on the dry powder by energy-dispersive X-ray fluorescence (EDXRF) using a Bruker Artax 200 spectrometer. The system was equipped with an X-ray tube (Mo anode) with a beam collimated down to 0.65 mm in diameter and using a 12.5 µm thick Mo transmission filter. The working conditions were 50 kV and 0.7 mA, with an acquisition time of 2700 s for each measurement. Bruker Spectra 5.1 software was used to perform peak deconvolution and error calculation. Relative atom concentrations were obtained using a NIST 610 as the standard reference material. (48) No evidence arises

of possible minor contaminations by other impurities, giving an upper limit of concentration of less than 20 ppm.

Results and Discussion

Because the size and shape potentially affect the nanocrystal surface energy and interaction with the surrounding environment, NCs endowed with different shapes and dimension have been synthetized for testing. Commercial TiO2 rutile samples, purchased from two different suppliers, anatase and brookite TiO2 NCs, synthesized by colloidal and solvothermal approaches, were fully characterized by means of TEM, DLS, XRD, ζ-potential, and BET after being stripped by their capping agents. The resulting characteristics are listed in Table 1.

Table 1. Crystal Dimensions Derived from XRD for Ana10 Calculated at (101) Peak, Bro40 at (120), and Rut20 and Rut50 at (110) Reported with Their Standard Deviation, TEM Reported with Their Standard Deviation, and DLS Measurements in Water Reported with Their Polydispersity Index (PDI)[a]

sample	XRD (nm)	TEM (larger dimension first)		DLS (nm)	PDI	BET specific surface area (m2 g–1)	predicted surface area (m2 g–1)	ζ-potential (mV)
Ana10	5.9 ± 0.4	7.6 ± 1.1		16	0.191	174 ± 7	197.4 ± 28.6	–27.8 ± 6.5
Rut20	4.6 ± 0.2	21.9 ± 3.3	4.0 ± 0.5	115	0.141	164 ± 7	141.1 ± 38.9	–31.0 ± 4.8
Bro40	5.6 ± 0.4	42.3 ± 7.5	3.5 ± 0.6	110	0.22	174 ± 7	154.2 ± 53.8	–29.3 ± 5.2
Rut50	13.3 ± 0.2	65.1 ± 7.8	30.0 ± 2.8	150	0.285	26 ± 7	20.4 ± 6.2	–17.7 ± 7.9

[a]BET specific surface areas as well as an estimate of surface area based on TEM size presented in the Supporting Information are reported with their standard deviation. ζ-Potential measured on water dispersions are reported with their standard deviation.

A direct investigation of stripped crystals size distribution and morphology is provided by TEM microscopy: representative images of the assemblies detected by sampling dispersions are presented in Figure 2.

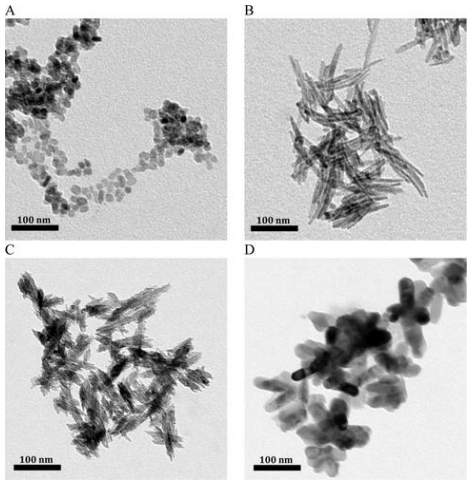

Figure 2. From top to bottom: TEM images of (A) Ana10, (B) Bro40, (C) Rut20, and (D) Rut50. All images were performed starting from highly dilute dispersions, indicating the extent of aggregation in the wet systems.

The TEM micrographs show that both the commercial rutile (Figure 2C,D) and brookite (Figure 2B) NCs have a rodlike morphology, whereas anatase (Figure 2A) has a quasi-spherical structure. It is possible to define the height and width of the crystals and with this information, using simple geometrical models, calculate the specific surface area for all samples. To get a complete picture of the NCs surface, the calculated specific surface areas are compared with the values obtained performing N2 adsorption (Table 1, BET), showing good agreement. All the NCs synthesized with OLAC as the capping agent were stripped in a ligand-exchange process and substituted with BF4– counterions, followed by a hydroxylation reaction with NH4OH. By removing OA, the surface becomes hydrophilic, thus enabling the transfer of NCs to water without affecting their size and shape, a fundamental aspect of our research. The DLS of the NCs in the three different stripping stages and the TEM pictures of the as-synthesized NCs and the stripped ones show that the size and shape are not affected by the ligand-exchange process (Figure S1). The effective replacement of organic ligands by inorganic BF4– anions is established by thermogravimetric analysis (TGA) and FTIR. In the IR spectra of the capped particle, Figure 3, the peaks associated with the aliphatic chain (3000–2750 cm–1) and the peaks of the antisymmetric and symmetric stretching of the carboxylate group (1520 and 1410 cm–1) are evident. The difference between the latter (~110 cm–1) is indicative of a chelating bidentate attachment of oleic acid on the surface. (24) In the stripped NCs spectra, the peaks related to the oleic acid aliphatic chain disappear, whereas the DMF peak appears (1640 cm–1) due to the fact that DMF acts as a NCs stabilizer and is weakly bonded to the titania surface. (4,52)

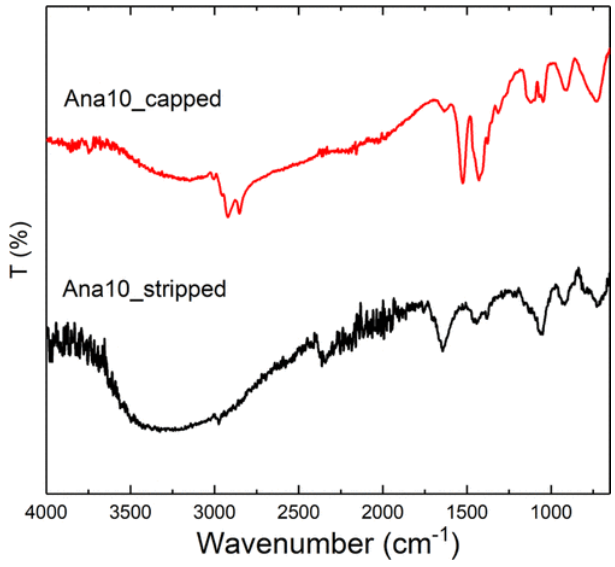

Figure 3. FTIR of capped (top, red) and stripped (bottom, black) anatase NCs. The lack of all adsorptions associated with the oleic acid molecules in the bottom spectrum indicates full stripping of the NP.

The TGA of the stripped NCs (Figure S2 in the Supporting Information) shows that between 150 and 600 °C, there is no more than 1% of organic material, indicating a fundamentally bare surface except for some absorbed residues that IR identifies as DMF. (45) Then, the crystallographic nature of the considered NCs has been verified by XRD as reported in Figure 4. All the reflections of the rutile commercial samples correspond to the ones of the bulk structure.

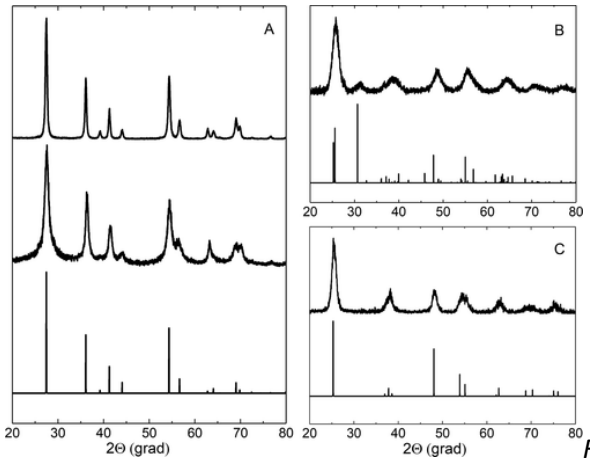

Figure 4

Figure 4. XRD diffractograms: (A) rutile, from top to down Rut50. Rut20 and rutile microcrystaline standard; (B) brookite, from top to down Bro40 and brookite microcrystalline standard; (C) anatase, from top to down Ana10 and anatase microcrystalline standard.

Diffractograms of NCs are also influenced by the crystal size, which causes a broadening in the diffraction lines: the broadening is inversely proportional to the crystal size. By analyzing the XRD data, indeed, it is possible to estimate the crystal dimensions using the Sherrer's formula

$$D = \frac{K\,\lambda}{B\,cos\theta}$$

(5)

where K is the shape factor, λ is the X-ray wavelength, B is the line broadening at half the maximum intensity, and θ represents the Bragg angle of the considered peak. Equation 5 was used to calculate the NCs' dimensions as reported in Table 1. The broadening due to the size effect is clear in the case of the Rut50 compared to the Rut20, the XRD pattern of the smaller rutile NCs appears broader than the larger one (Figure 4A). The XRD pattern of Ana10 corresponds to the standard one confirming the purity of the crystal phase (Figure 4B). The shape of the synthesized quasi-spherical anatase is confirmed by the XRD sizes analysis of the nanocrystal. A full calculation of the crystallite size along the different crystallographic directions has been done (Figure S3), showing homogeneous sizes along the different directions.

The brookite TiO2 crystal phase is instead characterized by a more complex XRD pattern. Here, the presence of significant broadening reduces the discriminating power of XRD: the main (101) diffraction peak of anatase at 2θ = 25.3° cannot be distinguished from the (120) and (111) peaks of brookite at 2θ = 25.3 and 25.7°, respectively. The only reliable indicator of the presence of brookite in the XRD patterns is the (121) peak at 2θ = 30.8°.

To fully confirm the composition of the brookite sample, as suggested by Buonsanti et al., (44) a Raman analysis was also performed. According with its greater crystal symmetry, the anatase vibrational spectrum is simpler if compared to the brookite spectrum. The overall spectral profile of brookite reported in literature is characterized by a very strong band at 158 cm–1 and a grouping of weaker bands at higher wavenumber. The most important distinction is around 400 cm–1. In this region, the brookite displays a peak at 421 cm–1, distinguishable from the anatase peak at 401 cm–1.

The spectra, presented in Figure 5, fully agree with literature examples. The insets in the figure shows that peaks at 399 and 419 cm–1 are present in the anatase and brookite, respectively, thus confirming the morphology of the samples.

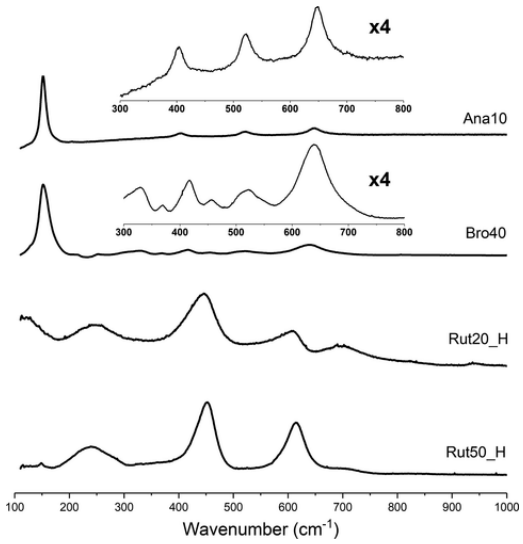

Figure 5. Raman spectra of TiO2 NCs. The rutile form is clearly distinguishable. The detected peaks at short wavenumber present in brookite and absent in anatase indicate the purity of the two samples.

To understand the behavior of the as-prepared NCs in a solution, an evaluation of the NCs' size in water dispersion is performed by DLS. The detected distributions of the hydrodynamic diameters are presented in Figure S4 (SI) for all the samples: they all indicate a rather low polydispersity index (PDI). The average hydrodynamic diameter values are reported in Table 1 and span from 16 to 140 nm, much larger than what is calculated from XRD probably due to the presence of aggregates.

The spherical approximations used in DLS tend to assign an apparent diameter close to the length of the longest axis of the elongated nanoparticles. Because differences between the DLS size and the expected single particles values are in excess of an order of magnitude, this factor alone is insufficient to justify the differences. A possible contribution to DLS hydrodynamic radius is particle aggregation: aggregates diffuse coherently and are revealed by the scattered light as single larger particles. This is a frequent phenomenon in case of small particles with a high surface energy, thus we checked its possible relevance by measuring the ζ-potential of all the NCs.

All the smaller particles, also reported in Table 1, provide results around −30 mV, indicating a stable colloidal dispersion; instead, the larger Rut50 particles display a smaller value of −17.7 mV.

Such ζ-potential values indicate a good stability of the NCs in water and thus suggest that the bonding between NCs within an aggregation is rather loose. The specific surface area calculated by BET, Table 1, on the basis of N2 adsorption on the centrifuged and dried NCs, is compatible with the theoretical specific surface area based on the TEM sizes. In other words, our assumption is that the entire NC surface is accessible by water when in dispersion.

The study of the surface properties through 1H-TD-NMR T2 relaxation has been performed using water as solvent. Because TiO2 NCs are known to be diamagnetic and thus do not cause NMR relaxation at long range, the theory for the NMR relaxation of protons of water molecules interacting with particle surfaces, described above, should hold as long as the solvent molecules bound to NCs surface are in fast exchange with the free ones.

To exclude the presence of metal traces that could be associated with the paramagnetic centers in the surface, EDXRF analysis was carried on each sample. As reported in Table 2, the metal content has broad variations between the different NCs, but is generally below 0.1% weight. Because there is no TEM evidence of an internal structuration of the NCs, it is expected that these amounts are dispersed within the sample and do not give rise to paramagnetic effects.

As described in the Experimental Section, TD-NMR data were acquired with the CPMG sequence, which acquires a signal intensity I(t) as a function of echo time. (3) All the curves, regardless of the particle type and concentration, could be well fitted with single exponential function $I(t) = I(0)\, e^{-(t/T2)}$, easily extracting the T2 relaxation time (Figure 6). This validates the fast-exchange model assumption and demonstrates the high accessibility of the surface. The presence of dense aggregates of NCs would generate a second population of water molecules with a different relaxation. No such population was detected.

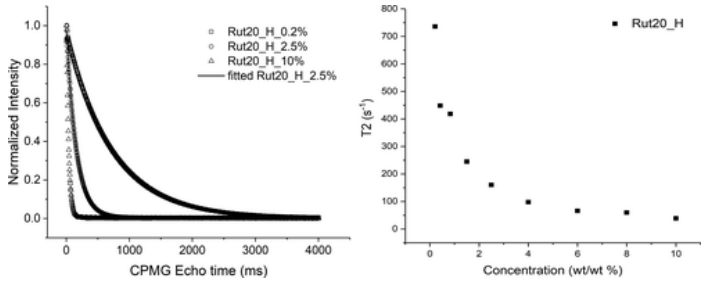

Figure 6. Left, example of monomodal fitting of the selected dispersions of Rut20 at different concentrations. Fitting lines are practically superimposed with the experimental data. On the right, the T2 values extracted from the CPMG experiments are plotted against the NP concentration.

For each NCs, R2 values equal to 1/T2 were obtained at several dilutions and plotted against the product of concentration and specific surface (σpCM). Figure 7 shows the evolution of R2 for water-dispersed rutile NCs, including the as-acquired commercial samples and their hydroxylated counterparts. All the samples were stable in water up to 6% w/w, allowing immediate measurement of R2 over an ample range of concentrations. All the data are fitted by linear functions with good correlation (r2 ~ 0.99), with slopes reported in Table 3. This indicates the particles are well dispersed, without tight aggregation phenomenon, which would modify the available surface as a function of the concentration, thus resulting in a nonlinear R2 function. Following eq 4, the slope is a measure of the interaction of water with the surface.

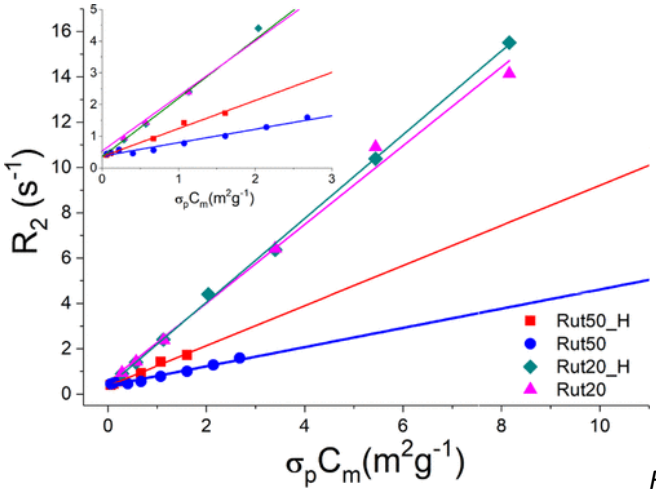

Figure 7

Figure 7. R2 of particles with and without the hydroxylation treatment, indicated with the suffix _H. R2 is expressed as function of available surface per gram of solution: Rut50_H, red square (red box solid); Rut50, blue circle (blue circle solid); Rut20_H, green diamond (green diamond solid); and Rut20, pink triangle (pink triangle up solid). Inset graph shows a much more detailed picture of the region at low σpCM.

Table 2. Metal Trace Concentrations (ppm in Weight) Resulting from EDXRF Analysis

sample	**Rut 20_H**	**Rut 50_H**	**Ana10**	**Bro40**
Ca	126 ± 24	33 ± 15	233 ± 30	590 ± 57
Fe	82 ± 13	6 ± 2	8 ± 3	24 ± 5
Zn	204 ± 92	389 ± 89	873 ± 141	222 ± 85
Hf	81 ± 59	582 ± 107	<20 (BdL)	142 ± 60

Table 3. Slopes of R2 as a Function of Normalized Surface for All Nanocrystals

sample	**slope**	**slope hydroxylated**
Ana10	0.51 ± 0.01	
Rut20	1.74 ± 0.08	1.85 ± 0.02
Bro40	0.54 ± 0.01	
Rut50	0.42 ± 0.03	0.88 ± 0.05

It is immediately apparent that slopes for smaller Rut20 particles are much steeper than those for Rut50, even after normalization against the specific surface measured by BET. This normalization removes the obvious R2 increase at a fixed weight concentration due to the increased surface-to-volume ratio of smaller nanoparticles. The slope after this correction is instead representative of the surface interaction.

Surface hydroxylation is expected to equalize the surface chemistry, and, in fact, it brings the samples closer in terms of relaxation behavior: as reported in Table 3, the slope of sample Rut20 is only marginally affected, whereas the effect of Rut50 on water relaxation is enhanced by about a factor 2. Even after this modification, the Rut20 sample composed by smaller particles still has a much higher specific R2, a first indication of the detailed insight that can be provided by the study of the water–particle interaction.

The hydroxylated rutile samples are replotted in Figure 8 together with anatase and brookite, whose surfaces are already hydroxylated due to our ligand-stripping process.

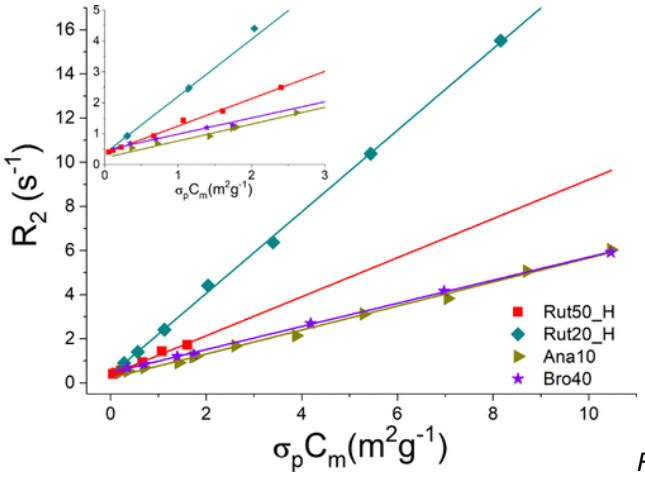

Figure 8

Figure 8. Comparison between R2 of rutile phase represented by Rut50_H, red square (red box solid); Rut20_H, green diamond (dark green tilted square solid); anatase Ana10 acid, green triangle (gray triangle right-pointing solid); and brookite Bro40, purple star (blue star solid). Inset graph shows a much detailed picture of the region at low σpCM.

Also, here, for all kinds of NCs, the R2 data fit with the linear model proposed. The most striking feature of this plot is that anatase and brookite display a very similar slope, much lower than even the larger rutile particles. Particularly, Rut50 has a slope of 0.88 ± 0.05 g m^{-2} s^{-1} and is remarkably different from both anatase and brookite. Anatase and brookite, instead, present similar behavior: their slopes are 0.51 ± 0.01 and 0.54 ± 0.01 g m^{-2} s^{-1}, respectively. All three polymorphs of TiO2 are therefore different from each other in terms of surface–water interaction, even though anatase and brookite are very close, making 1H-TD-NMR an informative tool for titania NCs characterization. In the framework of the equations presented above, the different particles are then distinguished by the factor µRb. The fact that the surface is clean from residual oleic acid allows us to relate the NMR relaxation behavior only to the NCs surface interaction with water.

As mentioned in the discussion, it is difficult to single out whether the higher R2 is due to higher relaxivity of the bound phase or by the greater number of binding sites per surface unit, especially considering that this investigation is based on exchange phenomena that average the interaction with the entire particle, a complementary approach to recent solid-state NMR investigations that focus on single facets. (49) Still, a correlation can be traced with the recently described interplay between surface energy, relative stability of the various polymorphs, and affinity with bound water. (50,51) Navrotsky et al. present surface energy as a function of particle size for all three polymorphs. It turns out that the functions for surface energies in the range of specific surface of our particles are in the same order as the µRb measured by us: brookite is slightly more energetic than anatase and rutile more than both. Even more interestingly, rutile has a very steep surface energy dependence on the surface area, in agreement with the increased interaction upon decrease in the rutile particle size (Rut50 to Rut20), even after normalization for specific surface and after

chemical equalization of the surface hydroxylation. These findings are yet qualitative, but they provide a basis for immediate applications in the characterization of the fine differences between particles of commercial origin or those produced from different methods, and further investigation of the mechanisms of water–surface interaction in the various polymorphs of titania is required.

Conclusions

Time domain NMR has been performed on water dispersions of NCs representing the three titanium dioxide crystal phases to quantitatively understand the interaction that occurs between their surfaces and water molecules. From the preliminary information given by XRD, Raman, and EDXRF analysis, the crystal phase and purity of each sample were verified. By combining the DLS, ζ-potential, TEM images, and BET data, we defined the size and shape of all the particles and verified the state of loose aggregation that they maintain in water. Thus, we could assume an equivalence between the amount of wet surface, the one actually interacting with water in dispersion, and the surface probed by nitrogen adsorption. Finally, we verified the full stripping and hydroxylation of titania surfaces and described the water 1H T2 relaxation times only in terms of interaction between water and different nanocrystal phases. By normalizing against the BET surface, we found a general agreement between the NMR specific R2 and the surface energy as presented for example by Ranade (52) because the values of brookite and anatase are very similar to each other and much smaller than those of rutile with similar specific surface. The R2 of rutile was also shown to increase with reduction in particle size, again in parallel with the evolution of surface energy as a function of rutile particle size. Finally, the NMR technique is also sensitive to surface treatment such as hydroxylation. Thus, along with other established and increasingly widespread methods for the shape and functionality determination by solvent relaxation, we have shown that with TD-NMR technique, it is possible to use water as a probe to identify different phases of the same oxide and crystals with different specific surface area and to obtain detailed information on the surface treatment.

(1) Issa, B.; Obaidat, I.; Albiss, B.; Haik, Y. Magnetic Nanoparticles: Surface Effects and Properties Related to Biomedicine Applications. Int. J. Mol. Sci. 2013, 14, 21266.

(2) Laurent, S.; Forge, D.; Port, M.; Roch, A.; Robic, C.; Vander Elst, L.; Muller, R. N. Magnetic Iron Oxide Nanoparticles: Synthesis, Stabilization, Vectorization, Physicochemical Characterizations, and Biological Applications. Chem. Rev. 2008, 108, 2064−2110.

(3) Vismara, E.; Bongio, C.; Coletti, A.; Edelman, R.; Serafini, A.; Mauri, M.; Simonutti, R.; Bertini, S.; Urso, E.; Assaraf, Y.; Livney, Y. Albumin and Hyaluronic Acid-Coated Superparamagnetic Iron Oxide Nanoparticles Loaded with Paclitaxel for Biomedical Applications. Molecules 2017, 22, No. 1030.

(4) Silva, A. C.; Oliveira, T. R.; Mamani, J. B.; Malheiros, S. M.; Malavolta, L.; Pavon, L. F.; Sibov, T. T.; Amaro, E., Jr.; Tannus, A.; Vidoto, E. L.; Martins, M. J.; Santos, R. S.; Gamarra, L. F. Application of hyperthermia induced by superparamagnetic iron oxide nanoparticles in glioma treatment. Int. J. Nanomed. 2011, 6, 591−603.

(5) Lee, B. G.; Luo, J.-W.; Neale, N. R.; Beard, M. C.; Hiller, D.; Zacharias, M.; Stradins, P.; Zunger, A. Quasi-Direct Optical Transitions in Silicon Nanocrystals with Intensity Exceeding the Bulk. Nano Lett. 2016, 16, 1583−1589.

(6) Champion, J. A.; Katare, Y. K.; Mitragotri, S. Particle shape: A new design parameter for micro- and nanoscale drug delivery carriers. J. Controlled Release 2007, 121, 3−9.

(7) Kim, J. S.; Kuk, E.; Yu, K. N.; Kim, J.-H.; Park, S. J.; Lee, H. J.; Kim, S. H.; Park, Y. K.; Park, Y. H.; Hwang, C.-Y.; Kim, Y.-K.; Lee, Y.- S.; Jeong, D. H.; Cho, M.-H. Antimicrobial effects of silver nanoparticles. Nanomedicine 2007, 3, 95−101.

(8) Choi, H. S.; Liu, W.; Misra, P.; Tanaka, E.; Zimmer, J. P.; Itty Ipe, B.; Bawendi, M. G.; Frangioni, J. V. Renal clearance of quantum dots. Nat. Biotechnol. 2007, 25, 1165−70.

(9) Pan, J.; Liu, G.; Lu, G. Q.; Cheng, H.-M. On the True Photoreactivity Order of {001}, {010}, and {101} Facets of Anatase TiO2 Crystals. Angew. Chem., Int. Ed. 2011, 50, 2133−2137.

(10) Li, Y.; Krentz, T. M.; Wang, L.; Benicewicz, B. C.; Schadler, L. S. Ligand engineering of polymer nanocomposites: from the simple to the complex. ACS Appl. Mater. Interfaces 2014, 6, 6005−6021.

(11) Salice, P.; Mauri, M.; Castellino, M.; De Marco, M.; Bianchi, A.; Virga, A.; Tagliaferro, A.; Simonutti, R.; Menna, E. Synthesis and characterisation of a trithiocarbonate for the decoration of carbon nanostructures. Chem. Commun. 2013, 49, 8048−8050.

(12) Kumar, S. K.; Jouault, N.; Benicewicz, B.; Neely, T. Nanocomposites with Polymer Grafted Nanoparticles. Macromolecules 2013, 46, 3199−3214.

(13) Alexandre, M.; Dubois, P. Polymer-layered silicate nanocomposites: preparation, properties and uses of a new class of materials. Mater. Sci. Eng., R 2000, 28, 1−63.

(14) Clift, M. J.; Rothen-Rutishauser, B.; Brown, D. M.; Duffin, R.; Donaldson, K.; Proudfoot, L.; Guy, K.; Stone, V. The impact of different nanoparticle surface chemistry and size on uptake and toxicity in a murine macrophage cell line. Toxicol. Appl. Pharmacol. 2008, 232, 418−427.

(15) O'Regan, B.; Gratzel, M. A low-cost, high-efficiency solar cell based on dye-sensitized colloidal TiO2 films. Nature 1991, 353, 737.

(16) Esthappan, S. K.; Kuttappan, S. K.; Joseph, R. Thermal and mechanical properties of polypropylene/titanium dioxide nanocomposite fibers. Mater. Des. 2012, 37, 537−542.

(17) Colombo, A.; Tassone, F.; Mauri, M.; Salerno, D.; Delaney, J. K.; Palmer, M. R.; Rie, R. D. L.; Simonutti, R. Highly transparent nanocomposite films from water-based poly(2-ethyl-2-oxazoline)/TiO2 dispersions. RSC Adv. 2012, 2, 6628−6636.

(18) Crippa, M.; Bianchi, A.; Cristofori, D.; D'Arienzo, M.; Merletti, F.; Morazzoni, F.; Scotti, R.; Simonutti, R. High dielectric constant rutile-polystyrene composite with enhanced percolative threshold. J. Mater. Chem. C 2013, 1, 484−492.

(19) Berberich, L. J.; Bell, M. E. The Dielectric Properties of the Rutile Form of TiO2. J. Appl. Phys. 1940, 11, 681−692.

(20) Reyes-Coronado, D.; Rodríguez-Gattorno, G.; EspinosaPesqueira, M. E.; Cab, C.; Coss, R.d.; Oskam, G. Phase-pure TiO2 nanoparticles: anatase, brookite and rutile. Nanotechnology 2008, 19, No. 145605.

(21) Uboldi, C.; Urban, P.; Gilliland, D.; Bajak, E.; Valsami-Jones,́ E.; Ponti, J.; Rossi, F. Role of the crystalline form of titanium dioxide nanoparticles: Rutile, and not anatase, induces toxic effects in Balb/3T3 mouse fibroblasts. Toxicol. In Vitro 2016, 31, 137−145.

(22) Weir, A.; Westerhoff, P.; Fabricius, L.; Hristovski, K.; von Goetz, N. Titanium Dioxide Nanoparticles in Food and Personal Care Products. Environ. Sci. Technol. 2012, 46, 2242−2250.

(23) Berne, B. J.; Pecora, R. Dynamic Light Scattering: With Applications to Chemistry, Biology, and Physics; Dover Publications, 2000.

(24) Thistlethwaite, P. J.; Hook, M. S. Diffuse Reflectance Fourier Transform Infrared Study of the Adsorption of Oleate/Oleic Acid onto Titania. Langmuir 2000, 16, 4993−4998.

(25) Wisser, F. M.; Abele, M.; Gasthauer, M.; Muller, K.; Moszner, N.; Kickelbick, G. Detection of surface silanol groups on pristine and functionalized silica mixed oxides and zirconia. J. Colloid Interface Sci.2012, 374, 77−82.

(26) Mroue, K. H.; Zhang, R. C.; Zhu, P. Z.; McNerny, E.; Kohn, D. H.; Morris, M. D.; Ramamoorthy, A. Acceleration of naturalabundance solid-state MAS NMR measurements on bone by paramagnetic relaxation from gadolinium-DTPA. J. Magn. Reson. 2014, 244, 90−97.

(27) Yamamoto, K.; Xu, J. D.; Kawulka, K. E.; Vederas, J. C.; Ramamoorthy, A. Use of a Copper-Chelated Lipid Speeds Up NMR Measurements from Membrane Proteins. J. Am. Chem. Soc. 2010, 132, 6929−6931.

(28) Johns, M. L.; Hollingsworth, K. G. Characterisation of emulsion systems using NMR and MRI. Prog. Nucl. Magn. Reson. Spectrosc. 2007, 50, 51−70.

(29) Bonetti, S.; Farina, M.; Mauri, M.; Koynov, K.; Butt, H. J.; Kappl, M.; Simonutti, R. Core@shell Poly(n-butylacrylate)@polystyrene Nanoparticles: Baroplastic Force-Responsiveness in Presence of Strong Phase Separation. Macromol. Rapid Commun. 2016, 37,584−9.

(30) Slichter, C. P. Principles of Magnetic Resonance; Springer: Berlin; New York, 1996.

(31) Ernst, R. R.; Bodenhausen, G.; Wokaun, A. Principles of Nuclear Magnetic Resonance in One and Two Dimensions; Oxford University Press: Oxford, 1987.

(32) Redfield, A. G. On the Theory of Relaxation Processes. IBM J. Res. Dev. 1957, 1, 19−31.

(33) Mears, S. J.; Cosgrove, T.; Thompson, L.; Howell, I. Solvent Relaxation NMR Measurements on Polymer, Particle, Surfactant Systems. Langmuir 1998, 14, 997−1001.

(34) Cosgrove, T.; Griffiths, P. C.; Lloyd, P. M. Polymer Adsorption. The Effect of the Relative Sizes of Polymer and Particle. Langmuir 1995, 11, 1457−1463.

(35) Letellier, M.; Tinet, D.; Maggion, R.; Fripiat, J. Study of relaxation mechanisms in clay/water systems. Determination of the surface area. Application to cements. Magn. Reson. Imaging 1991, 9, 709−716.

(36) Fairhurst, D.; Cosgrove, T.; Prescott, S. W. Relaxation NMR as a tool to study the dispersion and formulation behavior of nanostructured carbon materials. Magn. Reson. Chem. 2016, 54, 521−526.

(37) Karpovich, A. L.; Vlasova, M. F.; Sapronova, N. I.; Sukharev, V. S.; Ivanov, V. V. Determination of dimensions of exfoliating materials in aqueous suspensions. MethodsX 2016, 3, 19−24.

(38) Yuan, L.; Chen, L.; Chen, X.; Liu, R.; Ge, G. In Situ Measurement of Surface Functional Groups on Silica Nanoparticles Using Solvent Relaxation Nuclear Magnetic Resonance. Langmuir 2017, 33, 8724−8729.

(39) Gillis, P.; Peto, S.; Muller, R. N. Bound water in heterogeneous system relaxometry: An ill-defined concept. Magn. Reson. Imaging 1991, 9, 703−708.

(40) Valckenborg, R. M. E.; Pel, L.; Kopinga, K. Combined NMR cryoporometry and relaxometry. J. Phys. D: Appl. Phys. 2002, 35, 249.

(41) Fairhurst, D.; Prescott, S. The use of nuclear magnetic resonance as an analytical tool in the characterisation of dispersion behaviour. Spectrosc. Eur 2011, 23, 13−16.

(42) Cosgrove, T.; Jack, K. S.; Green, N.; Obey, T. M.; Wood, M. NMR Solvent Relaxation Studies on Concentrated Particulate Dispersions. In Supramolecular Structure in Confined Geometries; American Chemical Society, 1999; Vol. 736, pp 153−168.

(43) Dinh, C. T.; Nguyen, T. D.; Kleitz, F.; Do, T. O. Shapecontrolled synthesis of highly crystalline titania nanocrystals. ACS Nano 2009, 3, 3737−3743.

(44) Buonsanti, R.; Grillo, V.; Carlino, E.; Giannini, C.; Kipp, T.; Cingolani, R.; Cozzoli, P. D. Nonhydrolytic synthesis of high-quality anisotropically shaped brookite TiO2 nanocrystals. J. Am. Chem. Soc. 2008, 130, 11223−11233.

(45) Dong, A.; Ye, X.; Chen, J.; Kang, Y.; Gordon, T.; Kikkawa, J. M.; Murray, C. B. A generalized ligand-exchange strategy enabling sequential surface functionalization of colloidal nanocrystals. J. Am. Chem. Soc. 2011, 133, 998−1006.

(46) Jang, I.; Song, K.; Park, J. H.; Oh, S. G. Enhancement of dye adsorption on TiO2 surface through hydroxylation process for Dyesensitized solar cells. Bull. Korean Chem. Soc. 2013, 34, 2883−2888.

(47) Dollimore, D.; Spooner, P.; Turner, A. The bet method of analysis of gas adsorption data and its relevance to the calculation of surface areas. Surf. Technol. 1976, 4, 121−160.

(48) Pearce, N. J. G.; Perkins, W. T.; Westgate, J. A.; Gorton, M. P.; Jackson, S. E.; Neal, C. R.; Chenery, S. P. A Compilation of New and Published Major and Trace Element Data for NIST SRM 610 and NIST SRM 612 Glass Reference Materials. Geostand. Geoanal. Res. 1997, 21, 115−144.

(49) Li, Y.; Wu, X.-P.; Jiang, N.; Lin, M.; Shen, L.; Sun, H.; Wang, Y.; Wang, M.; Ke, X.; Yu, Z.; Gao, F.; Dong, L.; Guo, X.; Hou, W.; Ding, W.; Gong, X.-Q.; Grey, C. P.; Peng, L. Distinguishing faceted oxide nanocrystals with 17O solid-state NMR spectroscopy. Nat. Commun. 2017, 8, No. 581.

(50) Levchenko, A. A.; Li, G.; Boerio-Goates, J.; Woodfield, B. F.; Navrotsky, A. TiO2 Stability Landscape: Polymorphism, Surface Energy, and Bound Water Energetics. Chem. Mater. 2006, 18, 6324− 6332.

(51) Navrotsky, A. Energetics of nanoparticle oxides: interplay between surface energy and polymorphism. Geochem. Trans. 2003, 4, 34−37.

(52) Ranade, M. R.; Navrotsky, A.; Zhang, H. Z.; Banfield, J. F.; Elder, S. H.; Zaban, A.; Borse, P. H.; Kulkarni, S. K.; Doran, G. S.; Whitfield, H. J. Energetics of Nanocrystalline TiO2. Proc. Natl. Acad. Sci. U.S.A. 2002, 99, 6476−6481.